# An Introduction to Visualization of Diffusion Tensor Imaging and Its Applications

A. Vilanova[1], S. Zhang[2], G. Kindlmann[3], and D. Laidlaw[2]

[1] Department of Biomedical Engineering
   Eindhoven University of Technology, Eindhoven
   *a.vilanova@tue.nl*
[2] Department of Computer Science
   Brown University, Providence
   *{dhl,sz}@cs.brown.edu*
[3] School of Computing
   University of Utah, Salt Lake City
   *gk@cs.utah.edu*

**Summary.** Water diffusion is anisotropic in organized tissues such as white matter and muscle. Diffusion tensor imaging (DTI), a non-invasive MR technique, measures water self-diffusion rates and thus gives an indication of the underlying tissue microstructure. The diffusion rate is often expressed by a second-order tensor. Insightful DTI visualization is challenging because of the multivariate nature and the complex spatial relationships in a diffusion tensor field. This chapter surveys the different visualization techniques that have been developed for DTI and compares their main characteristics and drawbacks. We also discuss some of the many biomedical applications in which DTI helps extend our understanding or improve clinical procedures. We conclude with an overview of open problems and research directions.

## 1 Introduction

Diffusion tensor imaging (DTI) is a medical imaging modality that can reveal directional information in vivo in fibrous structures such as white matter or muscles. Although barely a decade old, DTI has become an important tool in studying white matter anatomy and pathology. Many hospitals, universities, and research centers have MRI scanners and diffusion imaging capability, allowing widespread DTI applications.

However, DTI data require interpretation before they can be useful. Visualization methods are needed to bridge the gap between the DTI data sets and understanding of the underlying tissue microstructure. A diffusion tensor measures a 3D diffusion process and has six interrelated tensor components. A volumetric DTI data set is a 3D grid of these diffusion tensors that form complicated patterns. The multivariate nature of the diffusion tensor and the

3D spatial characteristics of the diffusion tensor field combine to make DTI visualization a challenging task. It is early in the history of visualization of tensor fields and the field is still in an experimental stage. Visualization methods are exploring what users might need to see or evaluate qualitatively within the data. Any qualitative insights that result help identify quantitative measures that have statistical and scientific importance. Applications that involve visualization are beginning to be pursued, but they are even more embryonic than the visualization methods themselves.

This chapter describes current visualization techniques and analyzes their comparative strengths and weaknesses.

DTI research is broadly interdisciplinary. Figure 1 gives a simplified illustration of the research domains surrounding DTI. It is worth noting that all of the components in the diagram are interrelated: new discoveries in one specific area often lead to improvements in the whole DTI field. For example, Pierpaoli *et al.* found incorrect connections in the neural pathways generated from a DTI data set [1]. Issues like this stimulate research in diffusion imaging and lead to new methods, in this case high angular resolution imaging [2, 3].

In section 2, we review techniques for DTI data acquisition In section 3, we survey computational and visualization techniques. We review some applications of DTI in section 4, discuss some open issues and problems in section 5, and conclude in section 6.
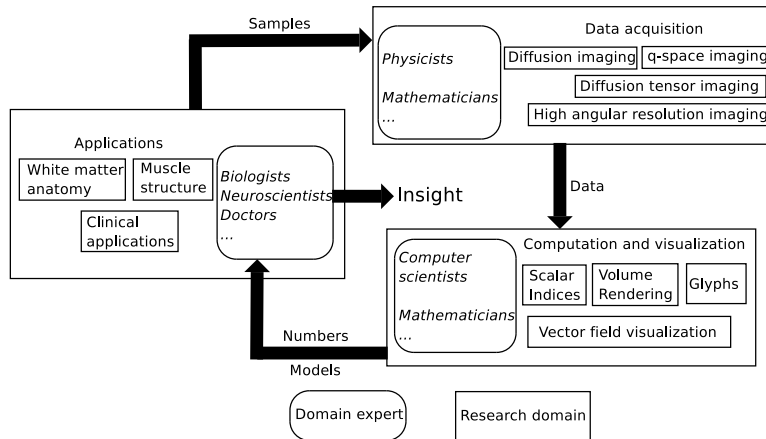


**Fig. 1.** The research context of DTI. Note that all the research domains are interrelated: progress in one domain can easily propagate to advance the rest of the field.

## 2 Diffusion Tensor Imaging

As for any visualization method, the merits of DTI visualization methods depend on the quality of the data. Understanding where the data come from, what they measure, and what their limitations are is an important first step in designing and implementing a visualization scheme. We briefly review the diffusion tensor imaging techniques here. Chapter 5 by Alexander presents a more detailed discussion of the subject.

Water molecules in human tissues constantly collide randomly with one another and with other molecules, a phenomenon called Brownian motion. In pure water, this seemingly random movement results in a dynamically expanding Gaussian distribution of water molecules released from one point [4]. In human tissues, however, cell membranes and large protein molecules limit the motion of water molecules. The geometrical and physical properties of the tissue determine the rate and orientation of diffusion. We can thus infer the microstructure of human tissue by measuring the diffusion of the water molecules.

The discovery of the nuclear magnetic resonance (NMR) effect [5, 6] in 1946 was the beginning of work that has led to the current form of diffusion magnetic resonance imaging (MRI). Two important landmarks were the discovery of the spin echo [7], whose signal is perturbed by the water molecule diffusion, and MR imaging [8], which determines exactly where the NMR signal originates within the sample. Diffusion imaging was the first imaging modality to measure the diffusion of water in human tissues in vivo. Although the exact mechanism of the generation of diffusion MRI signals in biological tissues is not fully understood, it is generally believed that the quantity measured by diffusion MRI is a mixture of intracellular diffusion, intercellular diffusion, and the exchange between the two sides of the the cell membrane [9].

Inferring tissue structure from the diffusion process requires exploring the orientation dependence of the diffusion. This dependence can be described by the diffusion propagator $P(r, r', \tau)$, which is the probability of a water molecule traveling from position $r'$ to $r$ in diffusion time $\tau$ [10]. In practice, the number of diffusion directions we can measure in a clinical scan is limited by scanning time, making it impossible to reconstruct the diffusion propagator completely. A diffusion tensor [11] describes the orientation dependence of diffusion assuming free diffusion in a uniform anisotropic medium (Gaussian diffusion). For example, a diffusion tensor is a good model for diffusion in uniformly oriented white matter structures such as the corpus callosum, but is insufficient in areas where different tracts cross or merge. The coefficients of the diffusion tensor, $\mathbf{D}$, are related to the diffusion-weighted MRI (DWI) signals by [12] $\tilde{I} = I_0 \exp(\mathbf{b} : \mathbf{D})$, where $I_0$ is the image with no diffusion weighting, the tensor $\mathbf{b}$ characterizes the diffusion-encoding gradient pulses used in the MRI sequence, and $\mathbf{b} : \mathbf{D} = \sum_{i=1}^{3} \sum_{j=i}^{3} \mathbf{b}_{ij} \mathbf{D}_{ij}$ is the tensor dot product.

A 3D diffusion tensor is a $3 \times 3$ positive symmetric matrix:

$$\mathbf{D} = \begin{bmatrix} \mathbf{D}_{xx} & \mathbf{D}_{xy} & \mathbf{D}_{xz} \\ \mathbf{D}_{xy} & \mathbf{D}_{yy} & \mathbf{D}_{yz} \\ \mathbf{D}_{xz} & \mathbf{D}_{yz} & \mathbf{D}_{zz} \end{bmatrix}$$

Diagonalizing $\mathbf{D}$, we get three positive eigenvalues $\lambda_1$, $\lambda_2$ and $\lambda_3$ (in decreasing order) and their corresponding eigenvectors $\mathbf{e_1}$, $\mathbf{e_2}$ and $\mathbf{e_3}$. Many scalar indices and visualization methods are based on the eigenvalues and eigenvectors of DTI measurements, as discussed in section 3.

One geometric representation of Gaussian diffusion is a diffusion ellipsoid. These ellipsoids represent the surface of constant mean-squared displacement of diffusing water molecules at some time $\tau$ after they are released from one point. The shape of a diffusion ellipsoid is inherently related to the eigenvalues and eigenvectors of the diffusion tensor: the three principal radii are proportional to the eigenvalues and the axes of the ellipsoid aligned with the three orthogonal eigenvectors of the diffusion tensor. Figure 2 shows ellipsoids representing different kinds of diffusion; the difference among the shapes of the ellipsoids are discussed in section 3.1.

DTI measurements have been validated within acceptable error on the fibrous muscle tissue of the heart [13, 14]. However, in a voxel containing nonuniformly oriented neural fibers (see figure 3), DTI measures an average signal from all the fibers within the voxel, which usually results in an apparent reduction of anisotropy and increase in uncertainty [15]. To resolve the
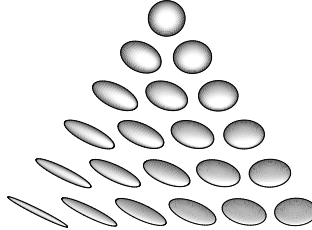


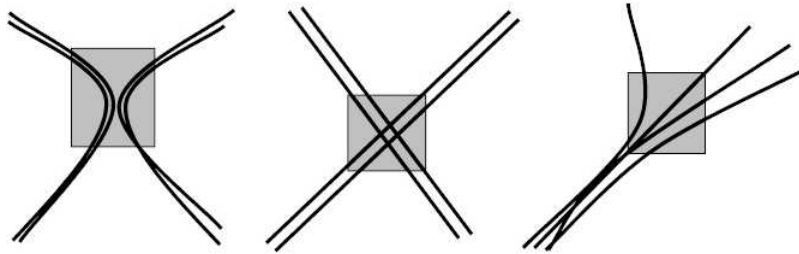**Fig. 2.** Barycentric space of diffusion tensor ellipsoids.



**Fig. 3.** Illustration of regions with planar anisotropy due to the fiber configuration. Gray regions represent voxels with planar anisotropy: (left) kissing fibers, (middle) two fiber bundles crossing and (right) diverging fibers.

uncertainty in these areas, $q$-space spectral imaging [16] and other high angular resolution diffusion imaging methods [17, 18] have been explored (see chapter 10 by zarslan et al.). Beyond these ambiguities introduced in regions where the diffusion is not coherent and cannot be modelled as a tensor, noise in the underlying MR images propagates through the computational pipeline changing the source diffusion weighted images, resulting diffusion tensor images, and visualizations based on them. Understanding the implications of all of these artifacts in visualizations is an active area of current research (see, e.g., chapter 6 by Hahn et al.).

Image acquisition for DTI is a very active research area. Progress is frequently reported on resolution improvement and reductions in imaging time, noise, and distortion.

## 3 DTI Visualization

Meaningful visualization of diffusion tensor fields is challenging because they are multivalued, with complex interrelationships among the values within a single tensor as well as among different tensors. The last decade has seen several approaches to visualizing diffusion tensor data, most of them based on reducing the dimensionality of the data by extracting relevant information from the tensor. One possible classification of the different visualization techniques is by the dimensionality to which the tensor is reduced. Another important characteristic is the ability of these algorithms to show local or global information, where global information means the complex spatial relationships of tensors. Our discussion here groups the visualization methods on the basis of these two criteria. Anisotropy indices reduce the 6D information to a scalar value (1D). *Volume rendering* for DTI uses anisotropy indices to define transfer functions that show the anisotropy and shape of the tensor. *Tensor glyphs* do not reduce the dimensionality of the tensor, instead using visual represntations that show the 6D tensor as such; however, these techniques cannot show global information. *Vector-field visualization* reduces the tensor field to a vector field, and therefore to 3D information at each point. Several techniques can be used for vector-field visualization that show local as well as global information. Section 3.5 describes algorithms in which the vector field is extended with more information from the tensor. This includes techniques where the whole tensor information is taken into account. Finally in section 3.6, several interaction schemes in DTI visualization are discussed.

### 3.1 Scalar Indices

The complexity of a DTI data set requires a complicated visualization scheme; however, medical researchers and practitioners alike are trained to read scalar fields on gray-level images slice by slice. Scalar data sets, although limited in the amount of information they can convey, can be visualized with simplicity

and clarity and thus interpreted quickly and easily. It can thus be useful to reduce DTI to scalar data sets. Since the advent of diffusion MRI, scalar indices of diffusion MRI data have been designed and visualized successfully alongside multivariate visualization schemes: rather than competing, the two methods complement one another.

The challenges of reducing a tensor-valued diffusion MRI measurement to a scalar index include mapping to a meaningful physical quantity, maintaining invariance with respect to rotation and translation, and reducing the effect of noise. Some scalar indices for DTI data are listed in Table 1.

| Scalar Index | Equations |
|---|---|
| Mean diffusivity, $\langle \mathbf{D} \rangle$ | $\dfrac{\mathbf{D}_{\mathrm{xx}} + \mathbf{D}_{\mathrm{yy}} + \mathbf{D}_{\mathrm{zz}}}{3}, \dfrac{\lambda_1 + \lambda_2 + \lambda_3}{3}, \dfrac{\mathrm{Trace}(\mathbf{D})}{3}$ |
| [19] Volume ratio, VR | $\dfrac{\lambda_1 \lambda_2 \lambda_3}{\left(\frac{\lambda_1+\lambda_2+\lambda_3}{3}\right)^3}, 27\dfrac{\mathrm{Determinant}(\mathbf{D})}{\mathrm{Trace}(\mathbf{D})^3}$ |
| [20] Fractional anisotropy, FA | $\sqrt{\dfrac{3}{2}}\dfrac{\|\mathbf{D} - \langle \mathbf{D}\rangle \mathbf{I}\|}{\|\mathbf{D}\|}$ |
| [20] Rational anisotropy, RA | $\dfrac{\|\mathbf{D} - \langle \mathbf{D}\rangle \mathbf{I}\|}{\|\langle \mathbf{D}\rangle \mathbf{I}\|}, \dfrac{\sqrt{\mathrm{Var}(\lambda)}}{\mathrm{E}(\lambda)}$ |
| [19] Lattice index, LI | $\displaystyle\sum_{n=1}^{N} a_n \left( \dfrac{\sqrt{3}}{\sqrt{8}} \dfrac{\sqrt{\mathbf{A}:\mathbf{A}_n}}{\sqrt{\mathbf{D}:\mathbf{D}_n}} + \dfrac{3}{4}\dfrac{\mathbf{A}:\mathbf{A}_n}{\sqrt{\mathbf{D}:\mathbf{D}}\sqrt{\mathbf{D}_n:\mathbf{D}_n}} \right)$ |
| [21] Linear anisotropy, $c_l$ | $\dfrac{\lambda_1 - \lambda_2}{\lambda_1 + \lambda_2 + \lambda_3}$ |
| Planar anisotropy, $c_p$ | $\dfrac{2(\lambda_2 - \lambda_3)}{\lambda_1 + \lambda_2 + \lambda_3}$ |
| Isotropy, $c_s$ | $\dfrac{3\lambda_3}{\lambda_1 + \lambda_2 + \lambda_3}$ |

Table 1: Some scalar indices for DTI data. $\|\mathbf{D}\| = \sqrt{\mathbf{D}:\mathbf{D}}$ is the tensor norm, $\mathrm{Var}(\lambda)$ and $\mathrm{E}(\lambda)$ are the variance and expectation of the three eigenvalues, $a_n$ is a normalized weighting factor, $\mathbf{A} = \mathbf{D} - \langle \mathbf{D}\rangle \mathbf{I}$.

Mean diffusivity (MD), which measures the overall diffusion rate, is the average of the diffusion tensor eigenvalues and is rotationally invariant. Van Gelderen *et al.* [22] demonstrated that, after a stroke, the trace of the diffusion tensor delineates the affected area much more accurately than the diffusion image in one orientation.

Before the diffusion tensor model was made explicit in 1994 by Basser *et al.* [11], several different anisotropy indices derived from DWIs were used, such as anisotropic diffusion ratio [23]. Unfortunately, these anisotropy indices depend on the choice of laboratory coordinate system and are rotationally vari-

ant: their interpretation varies according to the relative orientations of the MR gradient and the biological tissues, usually resulting in an underestimation of the degree of anisotropy [19]. Therefore it is important to use rotationally invariant anisotropy indices such as volume ratio (VR), rational anisotropy (RA) or fractional anisotropy (FA), which are based on the rotationally invariant eigenvalues. Note that both RA and FA can be derived from tensor norms and traces without calculating the eigenvalues.

However, rotationally invariant indices such as RA and FA are still susceptible to noise contamination. Pierpaoli *et al.* [19] calculated an intervoxel anisotropy index, the *lattice index* (LI), which locally averages inner products between diffusion tensors in neighboring voxels. LI decreases the sensitivity to noise and avoids underestimation of the anisotropy when the neighbor voxels have different fiber orientations.

Because they contract the tensor to one scalar value, FA, RA and LI do not indicate the directional variation of the diffusion anisotropy well. For example, a cigar-shaped and a pancake-shaped ellipsoid can have equal FA while their shapes differ greatly. Geometrical diffusion measures [21] have been developed: linear anisotropy, $c_l$, planar anisotropy, $c_p$ and spherical anisotropy or isotropy, $c_s$. By construction, $c_l + c_p + c_s = 1$. Thus, these three metrics parameterize a barycentric space in which the three shape extremes (linear, planar, and spherical) are at the corners of a triangle, as shown in figure 2. It is worth noting that, unlike FA or RA, geometrical diffusion metrics depend on the order of the eigenvalues and are thus prone to bias in the presence of noise [19].

Figure 4 shows one way to compare qualitatively some of the metrics described above by sampling their values on a slice of a DTI data set of a brain. Notice that the mean diffusivity (MD) is effective at distinguishing between cerebrospinal fluid (where MD is high) and brain tissue (lower MD),
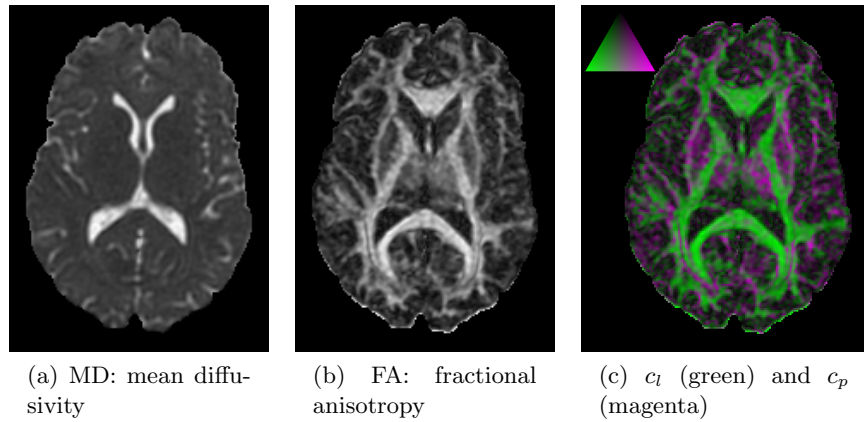


(a) MD: mean diffusivity

(b) FA: fractional anisotropy

(c) $c_l$ (green) and $c_p$ (magenta)

**Fig. 4.** Shape metrics applied to one slice of a brain DTI scan (see color plates).

but fails to differentiate between different kinds of brain tissue. High fractional anisotropy, FA, on the other hand, indicates white matter, because the directionality of the axon bundles permits faster diffusion along the neuron fiber orientation than across it. FA is highest inside thick regions of uniformly anisotropic diffusion, such as inside the corpus callosum. Finally, while both $c_l$ and $c_p$ indicate high anisotropy, their relative values indicate the shape of the diffusion ellipsoid.

### 3.2 Volume Rendering

Volume rendering is a means of visualizing large-scale structure in a tensor field, based on locally measured properties of the tensor data [24]. Volume rendering has the defining property of mapping from the tensor field attributes to a rendered image, without introducing additional geometry. However, volume rendering is inherently flexible in the sense that the volume scene can easily be supplemented with other visualizations (such as glyphs or fiber tracts, described in following sections) to create a more informative image. Compositing all the scene components together creates an integrated visualization in which local and global aspects of the field may be seen in context. The volume of tensor field attributes can either be precomputed and stored as a scalar field, or computed implicitly as part of rendering. In either case, an anisotropy index plays the important role of determining the opacity (thus visibility) of each sample. Each sample is then colored and shaded to indicate local shape characteristics; then samples are composited as the integral of colors and opacities are sampled along each ray.

An essential element of volume rendering is the *transfer function*, which assigns colors and opacities according to locally measured field properties. Traditionally, volume rendering has been applied to visualization of scalar fields, in which the domain of the transfer function is either the scalar value defining the data set or additionally includes derived quantities such as the gradient magnitude [25, 26]. The transfer function is usually implemented as a one-dimensional or two-dimensional lookup table. The transfer function domain variables are quantized to generate indices of table entries that contain the colors and opacity of the transfer function range.

The extension of volume rendering to diffusion tensor fields is thus essentially a matter of determining which quantities should serve as transfer function domain variables. To define opacity, the anisotropy indices in Table 1 are used. Fractional anisotropy (FA) is attractive in this respect because it can be expressed in terms of differentiable tensor invariants, so the chain rule can be used to calculate the gradient of FA as a normal for surface shading. Figure 5 shows a depiction of basic 3D structure with volume-rendered isosurfaces of fractional anisotropy. Rather than using a polygonal model of the anisotropy isosurface (as with Marching Cubes [27]), these images are computed with an opacity *step function*: opacity is 0.0 or 1.0 depending on whether FA is below or above the indicated threshold.
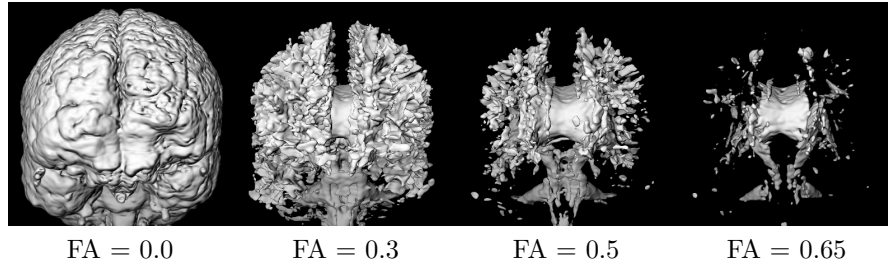
| FA = 0.0 | FA = 0.3 | FA = 0.5 | FA = 0.65 |

**Fig. 5.** Volume-rendered isosurfaces at a range of FA values show basic 3D structure of white matter in a DTI brain scan.

Color can be assigned in diffusion tensor volume rendering to indicate either the orientation or the shape of the underlying tensor samples. Applying the standard RGB coloring of the principal eigenvector (see section 3.4) allows basic neuroanatomic features to be recognized by their overall color, as in figure 6(a). Color can also be used to clarify differences in the shape of anisotropy apart from the anisotropy index used to define opacity. In particular, the difference between linear and planar anisotropy as measured by the $c_l$ and $c_p$ indices (Table 1) can be mapped onto the anisotropy isosurface, as in figure 6(b) (where the variation from green to magenta for linear to planar anisotropy is the same as in figure 4(c)). The rendering indicates how features with orthogonal orientations lead to planar anisotropy at their adjacencies. Locations in the brain characterized by this configuration of white-matter fibers include the right-left transpontine tracts ventral to the inferior-superior corticospinal tracts in the brainstem, and the right-left tracts of the corpus callosum inferior to the anterior-posterior cingulum bundles.
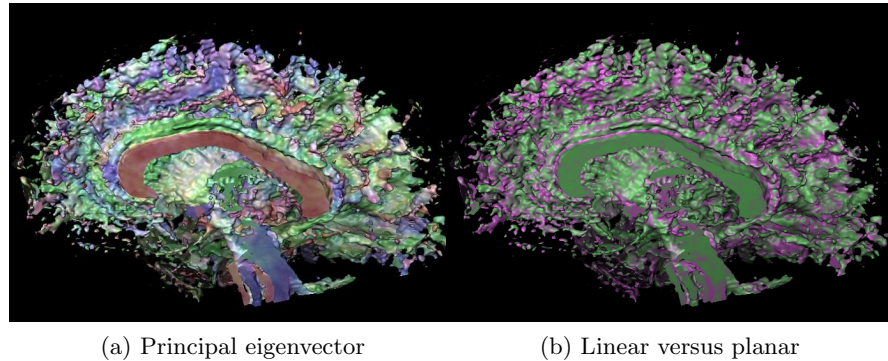


(a) Principal eigenvector             (b) Linear versus planar

**Fig. 6.** Volume renderings of half a brain scan, (a) colored according to orientation of principal eigenvector; (b) the distribution of linear (green) and planar (magenta) anisotropy. Surface is defined by FA = 0.4(see color plates).
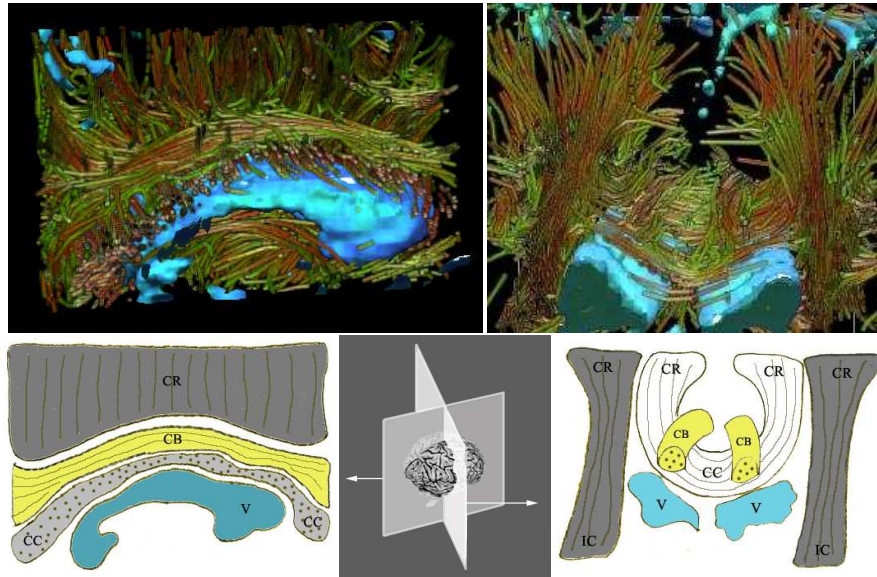
**Fig. 7.** Interactive volume renderings of a human brain data set. The volume renderings (top) show collections of threads consistent with major white-matter structures: IC=internal capsule, CR=corona radiata, CB=cingulum bundle, CC=corpus callosum diagrammed on the bottom. Components of the tensor-valued data control thread orientation, color, and density. Direct volume rendering simultaneously shows in blue the cerebral spinal fluid in the ventricles (labeled V) and some sulci for anatomical context(see color plates).

A recent application of volume rendering to diffusion tensor visualization is based on converting the tensor field to scalar fields, as described by Wenger *et al.* [28]. The approach here is to precompute multiple scalar volumes that can be layered and interactively rendered with 3D texture-mapping graphics hardware [29]. The renderings in figure 7 show visualizations that combine a volume rendering of the cerebral spinal fluid with a collection of fiber tracts rasterized into a color-coded scalar volume to illustrate the relationship between the distribution and orientation of the fiber tracts and the large-scale patterns of anisotropy. The flexible combination of the different scalar volumes into the final rendering permits interactive exploration and generation of visualizations.

There are currently no implementations that can volume render directly from a diffusion tensor volume to an image at interactive rates. The computational speed and flexibility of modern graphics hardware is increasing at such a rate, however, that this should soon be feasible. For example, two-dimensional transfer functions took minutes to render (in software) when introduced in 1988 [26], but can now be rendered at multiple frames per second with com-

modity graphics hardware [30]. Whether applied to scalar or tensor data, the intrinsically data-parallel nature of volume rendering makes it well suited to the streaming-based processors found on modern graphics hardware [31]. We anticipate that volume-rendering graphics hardware will play an increasing role in the interactive visualization of diffusion tensor data.

### 3.3 Tensor Glyphs

Another avenue of DTI visualization has focused on using tensor glyphs to visualize the complete tensor information at one point. A tensor glyph is a parameterized graphical object that describes a single diffusion tensor with its size, shape, color, texture, location, etc. Most tensor glyphs have six or more degrees of freedom and can represent a diffusion tensor completely. However, tensor glyphs do not expose relationships and features across a diffusion tensor field; rather, they imply these relationships from the visual correlation and features of the individual glyphs. While exploiting many different types of tensor glyphs, from boxes to ellipsoids to superquadrics, tensor glyph designers aim to make the mapping between glyphs and diffusion tensors faithful, meaningful and explicit.

The diffusion ellipsoid described in section 2 is the most commonly used representation of a diffusion tensor. Pierpaoli *et al.* [19], in the first use of ellipsoids as tensor glyphs for DTI, associated ellipsoid size with the mean diffusivity and indicated the preferred diffusion orientation by the orientation of the diffusion ellipsoid. Arrays of ellipsoids were arranged together in the same order as the data points to show a 2D slice of DTI data.

Laidlaw *et al.* normalized the size of the ellipsoids to fit more of them in a single image [32] (see figure 8(a)). While this method forgoes the ability to show mean diffusivity, it creates more uniform glyphs that show anatomy and pathology over regions better than the non-normalized ellipsoids.
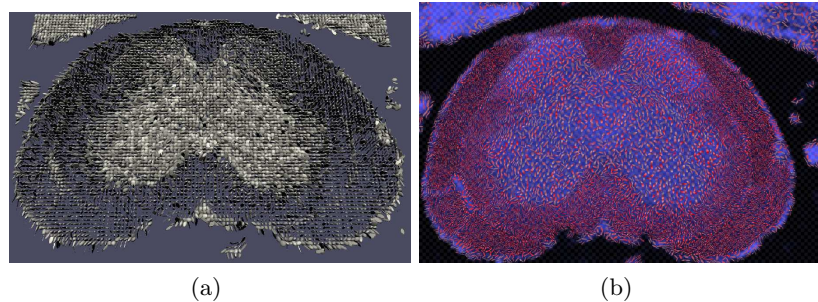


(a)                                      (b)

**Fig. 8.** (a) Arrays of normalized ellipsoids visualize the diffusion tensors in a single slice. (b) Brush strokes illustrate the orientation and magnitude of the diffusion: background color and texture-map show additional information(see color plates).
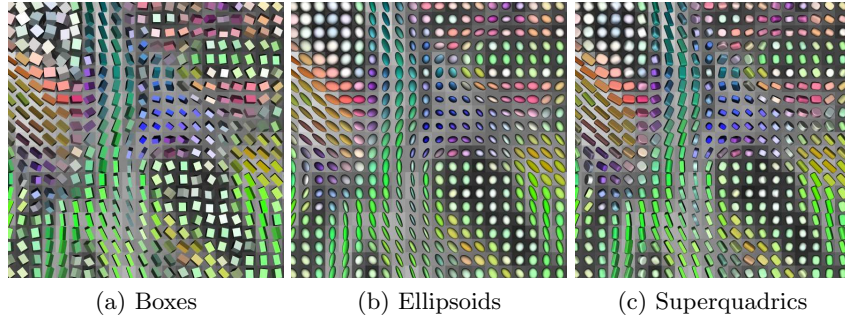
(a) Boxes                    (b) Ellipsoids                    (c) Superquadrics

**Fig. 9.** A portion of a brain DTI scan as visualized by three different glyph methods (overall glyph sizes have been normalized)(see color plates).

Laidlaw *et al.* [32] also developed a method that uses the concepts of brush strokes and layering from oil painting to emphasize the diffusion patterns. They used 2D brush strokes both individually, to encode specific values, and collectively, to show spatial connections and to generate texture and a sense of speed corresponding to the speed of diffusion. They also used layering and contrast to create depth. This method was applied to sections of spinal cords of mice with experimental allergic encephalomyelitis (EAE) and clearly showed anatomy and pathology (see figure 8(b)).

Boxes and cylinders have also been used to show the directions and relative lengths of all three eigenvectors. Boxes clearly indicate the orientation of the eigenvectors. They also have fewer polygons and are thus faster to render. But their flat faces usually make it hard to infer the 3D shapes from a 2D image (see figure 9(a)).

Kindlmann adapted superquadrics, a traditional surface modeling technique, to generate tensor glyphs [33]. The class of shapes he created includes spheres in the isotropic case, while emphasizing the differences among the eigenvalues in the anisotropic cases. As shown in figure 10, cylinders are used
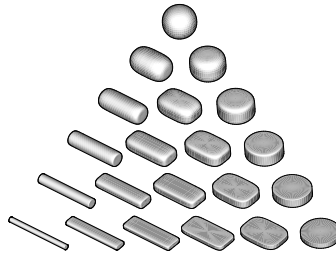


**Fig. 10.** Superquadrics as tensor glyphs, sampling the same barycentric space as in figure 2.

for linear and planar anisotropy and intermediate forms of anisotropy are represented by approximations to boxes. As with ellipsoid glyphs, a circular cross-section accompanies equal eigenvalues, for which distinct eigenvectors are not defined.

The differences among some of the glyph methods can be appreciated by comparing their results on a portion of a slice of a DTI brain scan, as shown in figure 9. The individual glyphs have been colored with the principal eigenvector colormap. The directional cue given by the edges of box glyphs 9(a) is effective in linearly anisotropic regions, but can be misleading in regions of planar anisotropy and isotropy, since in these cases the corresponding eigenvectors are not well defined numerically. The rotational symmetry of ellipsoid glyphs 9(b) avoids misleading depictions of orientation, with the drawback that different shapes can be difficult to distinguish. The superquadric glyphs 9(c) aim to combine the best of the box and ellipsoid methods.

### 3.4 Vector Field Visualization

The tensor field can also be simplified to a vector field defined by the main eigenvector, $\mathbf{e_1}$. This simplification is based on the assumption that in the areas of linear anisotropy, $\mathbf{e_1}$ defines the orientation of linear structures. The sign of $\mathbf{e_1}$ has no meaning.

One commonly used method to visualize DTI data is to map $\mathbf{e_1}$ to color, e.g., directly using the absolute value of the $\mathbf{e_1}$ components for the RGB channel: $R = |\mathbf{e_1} \cdot \mathbf{x}|$, $G = |\mathbf{e_1} \cdot \mathbf{y}|$, $B = |\mathbf{e_1} \cdot \mathbf{z}|$. The saturation of this color is weighted by an anisotropy index to de-emphasize isotropic areas (see figure 11).
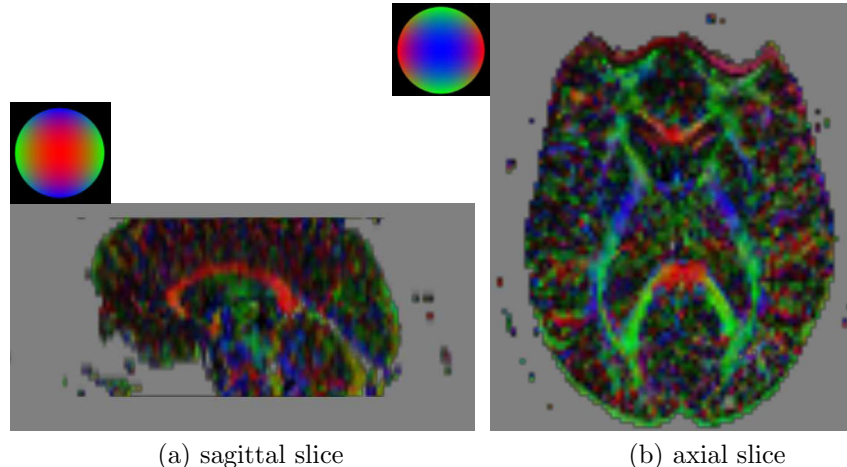


(a) sagittal slice                    (b) axial slice

**Fig. 11.** Mapping of $\mathbf{e_1}$ to the RGB channel shown in 2D slices of a healthy volunteer brain(see color plates).
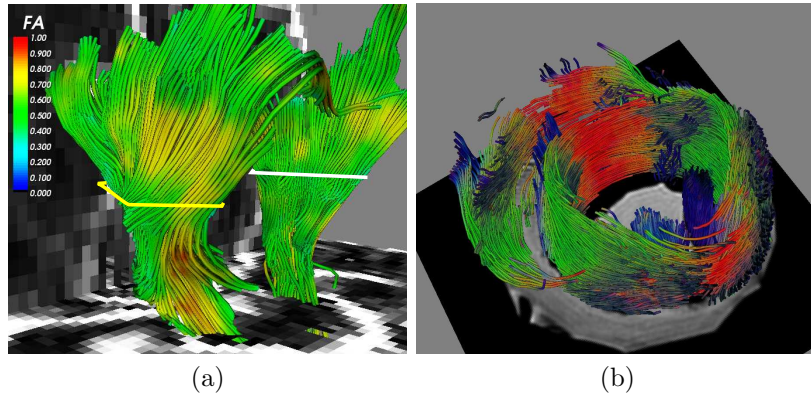
**Fig. 12.** (a) Streamline tracing using two ROIs to trace the corona radiata in a data set of a healthy volunteer brain. (b) Streamlines in a data set of a goat heart using the seeding technique of Vilanova *et al.* [38](see color plates).

Other methods have been proposed to visualize the global information of 2D as well as 3D vector fields [34], and there are well established 2D vector-field visualization methods [35]. Although 2D techniques have been extended to 3D, the visualization of 3D vector fields is still a challenging problem due to visual cluttering and computational cost.

We concentrate here on 3D DTI data. The most commonly used technique to visualize DTI data is streamline tracing; in DTI-specific literature this is also called fiber tracking [36] or tractography [37]. There is a direct analogy between the streamlines and the linear structures to be visualized (e.g., fibers). Furthermore, streamlines in 3D can easily be visualized by regions in order to avoid cluttering. Streamline tracing is based on solving the following equation:

$$p(t) = \int_0^t \mathbf{v}(p(s))ds \qquad (1)$$

where $p(t)$ is the generated streamline and $\mathbf{v}$ corresponds to the vector field generated from $\mathbf{e_1}$. $p(0)$ is set to the initial point of the integral curve.

The streamline technique has three main steps: definition of initial tracking points (i.e., seed points), integration, and the definition of stopping criteria. Seed points are usually user defined: the user specifies one or more regions of interest (ROI). Interior of the ROIs are sampled and the samples are used as seed points (see figure 12). Equation (1) is solved by numerical integration via such schemes as Euler forward and second or fourth-order Runge-Kutta. Stopping criteria avoid calculation of the streamline where the vector field is not robustly defined. In areas of isotropic or planar diffusion, the value of $\mathbf{e_1}$ can be considered random, and thus has no meaning for the underlying structure. The user can usually set a threshold based on the anisotropy indices (e.g., FA, RA or $c_l$) to describe the areas where the vector field is defined;

the value of this threshold depends on the data-acquisition protocol and the nature of the object being scanned. Other criteria can also be used, such as the curvature or length of the streamline.

Hyperstreamlines are an extension to streamlines for second-order tensor fields [39], first used by Zhang et al. for DTI data [40]. Hyperstreamlines employ all eigenvalues and eigenvectors. A streamline defines the axis of a generalized cylinder whose cross-section perpendicular to the axis is an ellipse defined by $e_2$ and $e_3$ and $\lambda_2$ and $\lambda_3$, respectively.

Streamline-tracing techniques for DTI have several disadvantages that are constantly being addressed. In areas of nonlinear diffusion the main eigenvector is not robustly defined [15]. However, linear structures can be present in areas with nonlinear diffusion, appearing where the linear structure orientation is not coherent within a voxel (see figure 3) or arising from noise. Most DTI tracing algorithms consider only the areas where the vector field is defined robustly. Several authors have proposed methods to trace within areas of isotropic or planar diffusion following the most probable diffusion orientation based on some heuristics (e.g., [41, 42]). Some of these methods are based on regularization techniques that are commonly used in image processing for noise removal.

Another difficulty in streamlines is seeding. The seed points can be defined by the user. In a healthy person with known anatomy, users can estimate where the interesting bundles are and where to seed. However, in some cases, there are no real clues to the possible underlying structure and user seeding can miss important structures. Defining the seed points to cover the whole volume can be computationally expensive, however, and furthermore, too many seed points clutter the image and make it difficult to extract useful information.

Zhang *et al.* [40] employed uniform seeding throughout the entire volume and developed a culling algorithm as a postprocessing step to control the streamline density. This allows inside structures to be visible and outside structures still to be adequately represented. The metrics for the culling process include the length of a trajectory, the average linear anisotropy along a trajectory, and the similarity between a trajectory and the group of trajectories already selected.

Vilanova *et al.* [38] extended Jobard *et al.*'s seeding algorithm [43] for 3D DTI data (see figure 12(b)). Here seeding and generation of streamlines depend on a parameter that defines the density of the streamlines (i.e., minimal distance between streamlines). This method allows control of cluttering and less computationally expensive generation of streamlines than seeding the whole volume regularly. However, if the density is set to a low value this method does not guarantee that the important structures are visible, since only the distance between streamline seed points is taken into account.

Generally, the fiber bundles are more interesting than an individual fiber, and several authors have proposed ways to cluster the streamlines to obtain bundles (e.g., [44, 45, 46, 47]). These algorithms differ primarily in the metrics used to define the similarity between streamlines and clusters, which

are mainly based on the shape and distance between fiber pairs. Bundles are a compact representation of the data that alleviates cluttering; however, these algorithms have the disadvantage of relying solely on the results of the streamline-tracing algorithm, and therefore are very sensitive to its errors.

## 3.5 Beyond Vector Field Visualization

The previous section presented several visualization methods for which the diffusion tensor data are simplified to the main diffusion orientation to reconstruct the underlying linear structure. In doing this, of course, information is lost. In this section, we present several approaches that try to rectify this loss and use more information than the main eigenvector, $\mathbf{e_1}$. In DTI, it is
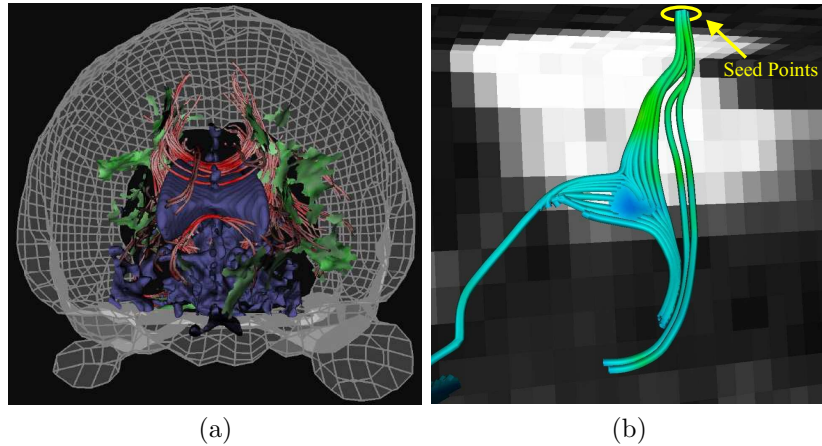


(a)                           (b)

**Fig. 13.** Examples of streamsurfaces: (a) red streamlines (represented as cylinders) and green streamsurfaces generated using the method of Zhang *et al.* [40] show linear and planar anisotropy, respectively, together with anatomical landmarks for context; (b) Streamlines using seed points (yellow region) trace streamsurfaces and show the possible prolongation of the fiber bundle, generated using the algorithm of Vilanova *et al.* [38](see color plates).

assumed that the diffusion tensor gives an indication of the underlying geometrical structure. In the streamline tracing algorithm, the main eigenvector is assumed to represent the tangent vector of an underlying linear structure. However, diffusion does not indicate just linear structures, but also planar structures (e.g., sheet). Similarly to linear anisotropy, it can be assumed that planar anisotropy indicates a planar structure. Therefore, the eigenvectors $\mathbf{e_1}$ and $\mathbf{e_2}$ define the tangent plane of an underlying planar structure, i.e., the streamsurface. Zhang *et al.* [40] presented an algorithm to generate the

streamsurface based on the planar anisotropic characteristics of the data. Figure 13(a) shows the results of using their algorithm to trace streamlines and streamsurfaces in the whole volume. In the brain there are no structures which have a planar like shape. However, due to fibers crossing and the partial volume effect planar like structures appear in the DTI data. Vilanova *et al.* [38] used a similar algorithm to Zhang et al. in combination with streamline tracing to show the areas where linear structures cross, kiss, converge or diverge (see figure 3).

Figure 13(b) shows streamlines generated by a few seed points (in the yellow circle). Instead of stopping, a streamsurface is traced when a streamline reaches an area of planar anisotropy. In addition, the possible continuations of the initial streamline going through the streamsurface are traced further.

Streamsurfaces are extensions of streamlines, but the tensor information is still simplified and not treated as a whole. Parker *et al.* [48] and Brun *et al.* [49] modeled all possible paths from a given starting point. Parker *et al.* used a front-propagation method with a speed function based on the underlying tensor field. The path between the starting point and any point in the volume is defined by using the time of arrival of the front to each point and a gradient-descent algorithm. A connectivity metric describes the likelihood of connection of each path. Brun *et al.* [49] modeled the paths as a probability distribution that is discretely represented by weighted samples from it. For each path, a connectivity is also assigned according to the diffusion tensor and the path's shape. Batchelor *et al.* [50] propose a method based on simulating the diffusion defined by the diffusion tensor, and use a probabilistic interpretation of the time of arrival of the diffusion front to quantify the connectivity of two points. O'Donnell *et al.* [51] describe a similar idea: a flux vector field based on solving for the steady-state concentration is created. Paths generated in this vector field have a measure of connectivity based on the flow along the paths; the maximum flow indicates the most probable connection. They also present a method based on warping the space locally using a metric defined by the inverse of the diffusion tensor. The minimum-distance path (i.e., geodesic) in this warped space provides a reconstruction of a possible underlying linear structure and a numerical measure of connectivity between two points (i.e., distance).

The advantage of these methods is that they are well defined in the complete space, even in areas with planar or isotropic diffusion. Furthermore, they give a quantitative measure of connectivity. Their drawbacks are that they are computationally expensive and any pair of points in the space is connected. Therefore, it is necessary to define not just a starting point but also end points, or to establish criteria for which points are considered to be connected (e.g., a percentile of the most probable connections).

There have been several efforts to visualize the global information of the second-order tensor field in general [52, 53] ( see also chapter 16 by Hotz et al.). Zheng and Pang [54] presented an extension of the vector-field visualization method LIC (line integral convolution) to tensor data. Similarly, Bhalerao and

Westin [**?**] extended splatting (a scalar volume rendering technique) to tensor data. Cluttering is a problem when these methods are applied to DTI data, since not much more than the outer shell of the anisotropic areas is visible.

Hesselink *et al.* [55] presented a method to extract topology skeletons of second-order 3D tensor fields. These skeletons are mainly defined by points, lines and surfaces that represent the complex structure of a tensor field in a compact and abstract way. The topology is based on the calculation of degenerate points whose eigenvalues are equal to each other. In chapter 14, Zheng et al. show that the stable degenerated features in 3D tensor fields form lines. The main drawback of this method is the lack of an intuitive interpretation of the topology skeletons for tensor fields. In real data, the resulting skeletons can be very complex and difficult to analyze.

## 3.6 Interaction

Human-computer interaction (HCI) arises in multiple aspects of DTI visualization: transfer function manipulation, seeding point selection, streamline culling, streamline query, and graphical model exploration, to name a few. We briefly review some of the interaction techniques here. In volume rendering,
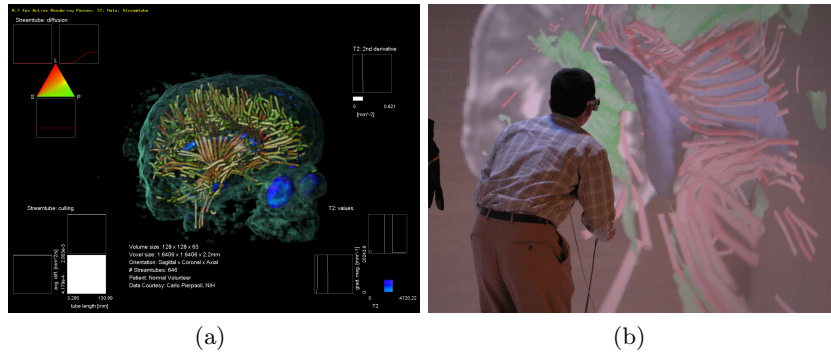


(a)                                    (b)

**Fig. 14.** (a) An interactive exploration tool for DTI volume rendering. Clockwise from upper left are a 2D barycentric widget, a 1D widget, a 2D Cartesian widget, and a 2D Cartesian culling widget. (b) A user explores a complex 3D model in a virtual reality CAVE(see color plates).

transfer functions determine the mapping from the data to color and opacity (see section 3.2). The selection of transfer functions often requires expertise; in addition, it is often done by trial and error, so that it is important that the user be able to select the transfer functions intuitively and quickly. Kniss *et al.* [30] describes a set of widgets that let the user specify multidimensional transfer functions interactively. Wenger *et al.* [28] applied this idea to DTI

volume rendering, employing a set of widgets including a barycentric widget for manipulating the geometrical diffusion measures (see figure 14).

Interaction permeates the whole process of vector field visualization: both seed points selection and connectivity query involve specifying ROIs. Streamline culling requires selecting certain criteria and setting the corresponding thresholds. Displaying the 3D streamline models often relies on user input to show the models at different scales and perspectives. Akers *et al.* [56] developed a pathway-query prototype to expedite the first two operations, precomputing the pathways and their statistical properties to achieve real-time interaction.

The complexity of the DTI data sets often yields complicated graphical models that are hard to discern in a still picture. Continuing developments in computer graphics constantly change how users interact with these models. Desktop 3D graphics used mouse click and drag to move the models; fishtank virtual reality display systems added stereo and head tracking [57]. The CAVE provided an immersive virtual environment that engaged the user in whole-body interaction [58] (see figure 14(b)). However, none of these systems are sufficient alone; each has its strengths and weaknesses depending on certain applications [57].

The interaction schemes can also be combined in hybrid visualization methods. For example, the streamtube-culling widget can be incorporated into the control panel with various other transfer function widgets (see figure 14(a)). A traditional 2D structural image slice provides context in a complex 3D scene (see figure 14(b)).

Currently, computational power limits our ability to achieve real-time interaction and precomputed models must often be used for sake of speed. In the future, we expect a closer tie between computation and human input for more efficient and effective data exploration.

## 4 Applications

DTI is especially useful in studying fibrous structures such as white matter and muscle: the anisotropy information it provides reveals the fiber orientation in the tissue and can be used to map the white-matter anatomy and muscle structure in vivo [37]. The diffusion coefficient measures a physical property of the tissue and the measurements can be compared across different times, locations, and subjects. Therefore, DTI has frequently been used to identify differences in white matter due to a variety of conditions. Normal conditions such as age and gender have been reported to affect anisotropy and diffusivity; neural developments such as myelination, physical trauma such as brain injury, and neurodegenerative diseases such as multiple sclerosis and HIV have all been indicated by DTI studies to affect white-matter composition, location, or integrity.

The variety of DTI applications provides a valuable testbed for visualization methods. Indeed, without applications to guide the development of computational and visualization tools, these tools are far less likely to be useful. We introduce some of the applications of DTI in this section.

## 4.1 White Matter Normal Conditions

Some normal conditions are reflected in the microstructure of white matter. Significant differences were found in diffusivity and anisotropy of the human corpus callosum with gender and handedness [59]. Age also has significant effect on white matter, usually resulting in reduced FA and increased diffusivity [60, 61]. These factors should be considered when selecting control groups for white-matter pathology studies.

The vector-field visualization methods introduced in section 3.4 have been employed to reveal connectivity in a normal brain. A common application is to use neuroanatomy knowledge to select ROIs and then reconstruct neural pathways running through them. Evidence of occipito-temporal connections within the living human brain was found by tracing neural pathways between two ROIs [62]. Expert-defined ROIs for brainstem fibers and associated fibers have been used to generate corresponding tracts [63]. An exciting trend is to combine functional MRI (fMRI), which measures the changes in blood flow and oxygenation in a brain area, with DTI fiber tracking, so that both activated brain areas and the tract connecting them to other brain areas can be visualized at the same time. For example, foci of fMRI activation have been used as ROIs to reveal axonal connectivity in a cat's visual cortex [64].

## 4.2 White Matter Development

Almost all the neurons that a brain will ever have are present at birth. However, the brain continues to develop for a few years after birth. A significant aspect of brain development is myelinization, the continued growth of myelin around the axons. Myelin acts as an insulating membrane and allows a conduction of nerve impulses from ten to one hundred times faster than along a non-myelinated system and, at birth, few fibers are myelinated. The development of myelin is thus a measure of increasing maturity of the neural system. Previous studies have explored when particular fibers are myelinated; e.g., areas related with primary sensory (vision, touch, hearing, etc.) and motor areas are the first to myelinate [65].

Diffusion tensor imaging has the potential to evaluate brain maturity in newborns. Myelinated fibers have higher anisotropy than non-myelinated ones, i.e., the anisotropy depends on the development phase. The study of newborn brain presents new challenges:

- The anisotropy in the neonatal brain is lower than in the adult brain. Therefore it is more difficult to reconstruct fibers reliably.
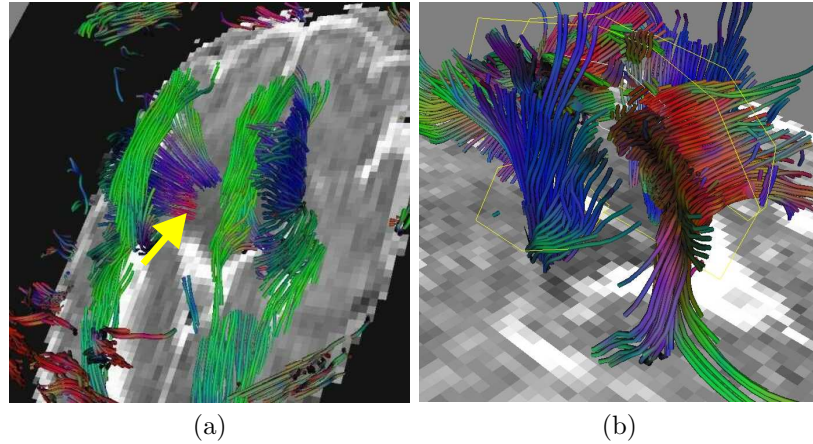
**Fig. 15.** Studies of white matter fibers in neonatal brains with different data sets. (a) Premature neonate lacking corpus callosum (see arrow), (b) full-term neonate where no fiber abnormalities were found. Corpus callosum and corona radiata are seen(see color plates).

- Motion artifacts can play a larger role, since neonates often move more than adults.
- The signal-to-noise ratio is smaller. The neonatal brain is smaller than that of an adult, and hence the voxel size must be smaller, leading to decreased signal.

The first years of life are a critical time for brain development. Early diagnoses of brain lesions can help diminish the consequences of an injury. For example, neonates who suffer hypoxic ischemic brain damage have brain injuries caused by lack of oxygen and nutrients because of blood flow problems. Diffusion weighted imaging has already proved useful in detecting this injury. Diffusion tensor imaging might provide further information about structure and the development of the neonatal brain. Figure 15(a) shows the white matter fibers corresponding to a data set of a premature neonate of 26 weeks and scanned at six weeks old. Several fiber structures are visible (e.g., corona radiata in blue). However, the corpus callosum is not visible: the arrow indicates where the fibers are missing. Further investigation of remaining MR images of this neonate confirmed that this patient lacks a corpus callosum. Figure 15(b) shows the result of tracing streamlines using ROIs to visualize the corpus callosum and the corona radiata in a full-term neonate scanned at four weeks after birth. The DTI data does not reveal any alteration in the fibers, even though the neonate had meningitis.

## 4.3 White Matter Injury and Disorders

DTI has proven effective in studying a range of white-matter disorders. Some of these disorders are brain injury, brain tumor, focal epilepsy, multiple sclero-

sis, tuberous sclerosis, Parkinson's disease, Alzheimer's disease, schizophrenia, HIV infection, Krabbe's disease, chronic alcohol dependence, ALS, X-linked ALD, and CADASIL. Reviews of these studies can be found in [66, 67, 68, 69]. We select three application areas in which pathological causes differ greatly, resulting in different patterns and subtleties of the changes in white matter. These cases can be analyzed effectively only by applying processing and visualization methods accordingly.

## Brain Tumor

It is estimated that 17,500 people in the U.S. die from primary nervous-system tumors each year [70]. A better understanding of the pathophysiology of brain tumors is essential if we are to find effective treatments. Cortical disconnection syndromes may play a significant role in clinical dysfunction associated with this disorder.

Tractography methods have been applied to study patterns of white-matter tract disruption and displacement adjacent to brain tumors. Wieshmann *et al.* [71] found evidence of displacement of white-matter fibers of the corona radiata in a patient with low-grade glioma when compared with spatially normalized data collected from 20 healthy volunteers. Mori *et al.* [72] found evidence of displacement and destruction of the superior longitudinal fasciculus and corona radiata in two patients with anaplastic astrocytoma. Gossl *et al.* [73] observed distortion of the pyramidal tract in a patient with
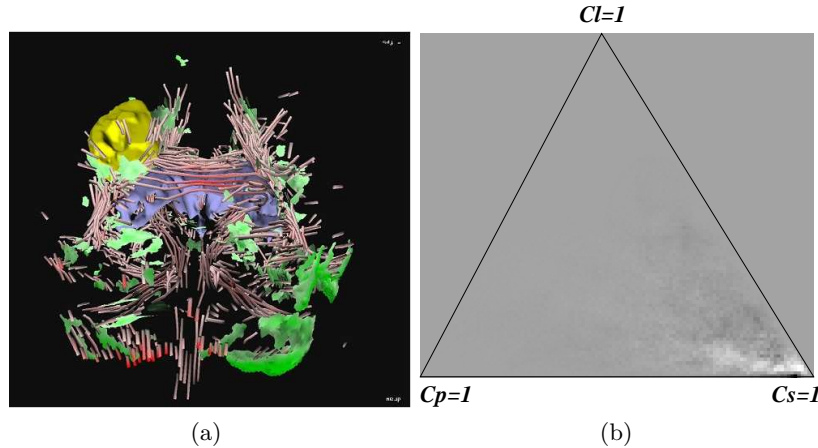


(a)                                                  (b)

**Fig. 16.** Visual exploration and quantitative analysis of a cancerous brain. (a) A 3D visualization showing streamtubes and streamsurfaces as well as tumor and ventricles. (b) The difference histogram obtained by subtracting normalized barycentric histograms calculated from tumor-bearing and contralateral sections. Here zero maps to medium gray because the difference is signed. Note that the most striking difference occurs near the $c_s = 1$ vertex(see color plates).

a high-grade glioma. Witwer *et al.* [74] found evidence of white-matter tract edema. Zhang *et al.* [75] observed the pattern of linear and planar diffusion around a tumor and analyzed the asymmetries of white-matter fiber tracts between the tumor and the contralateral hemisphere.

Figure 16 shows visual exploration and quantitative analysis of a cancerous brain [75]. The streamtubes and streamsurfaces visualize both linear and planar diffusion. The displacement of fiber tracts around the tumor is accompanied by a cradle of streamsurfaces, indicating a local increase of planar anisotropy. The normalized distribution of anisotropy is calculated on a barycentric space (see section 3.1) for both the tumor-bearing side and contralateral side of the brain. The difference in the two distributions (figure 16(b)) clearly indicates a decrease in linear anisotropy and an increase in planar anisotropy in the tumor side of the brain. As figure 17 indicates, the geometrical alteration of fiber structures surrounding the tumors can have different patterns [38]. In figure 17(a), the fibers are pushed to the left by the presence of the tumor; in figure 17(b), the fibers seem to be destroyed: the structure around the tumor is not moved, but in the tumor area no fibers are present.

Tumors and their surrounding edema often cause gross changes in the neural fibers around them. DTI can benefit tumor growth study and surgery planning by modeling these changes geometrically. Scalar index analysis complement the geometrical modeling by quantifying these changes.
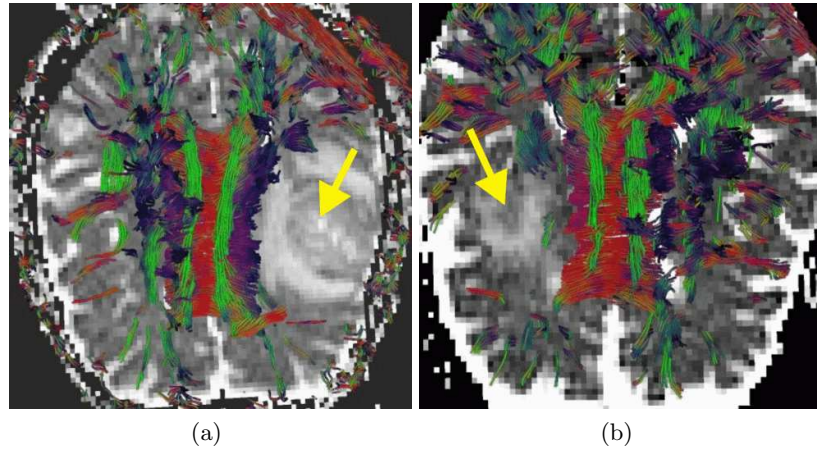


(a)                                         (b)

**Fig. 17.** Two cases of adult tumor brain. (a) Fibers are pushed by the tumor. (b) No fibers are in the tumor area, indicating the destruction of neural structures there(see color plates).
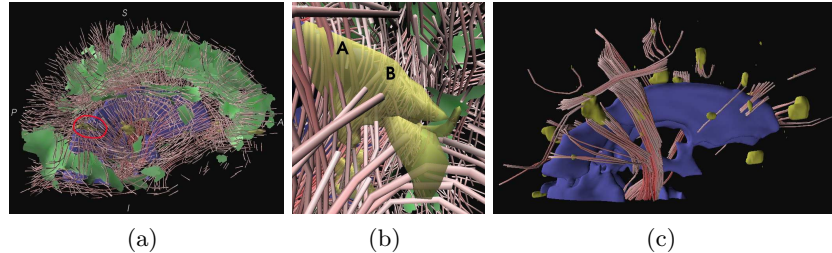
**Fig. 18.** Visualization of coregistered DTI and MS lesion models. (a) The whole brain with streamtubes, streamsurfaces, lesion masks and ventricles. (b) A closeup view of white matter fibers near the MS lesions. The streamtubes around the lesion area give some clues about white matter structural changes there. (c) The same brain and view as (a) but showing only streamtubes that contact the lesions, thus clarifying the white matter structures involved(see color plates).

### Multiple Sclerosis

Multiple sclerosis (MS) is a chronic disease of the central nervous system that predominantly affects young adults during their most productive years. Pathologically, MS is characterized by the presence of areas of demyelination and T-cell predominant perivascular inflammation in the brain white matter. Recent studies on MS have shown an elevated mean diffusivity and reduced diffusion anisotropy [76] in MS lesion areas. The lesions with more destructive pathology are generally shown to have the highest diffusivity.

Analyzing the interrelationship between the MS lesion and the affected fiber pathways might help in understanding the mechanism of the axonal damage. The visualization of DTI models with coregistered MS lesion masks in figure 18 can be utilized to determine the relationship between focal lesions and the neuronal tracts that are anatomically related. Figure 18(b) suggests the different effects that the focal lesions might have on the fibers. Note that the streamtubes sometimes continue through the lesions (A) and sometimes break within them (B). Figure 18(c) depicts only the fiber pathways that are confined in the lesion area.

MS lesions are often dispersed and show different levels of severity. Visualizing the affected tracts can clarify the various effects of the lesions. Identifying the gray matter to which these partially damaged tracts connect might help explain the disabling effect of MS. The study of MS remains an active research area. These visualization results might help researchers think about the progression of the pathology and design other experiments which, in turn, might help validate the DTI results.

### HIV Neurodegeneration

Human immunodeficiency virus (HIV) is an aggressive disease that affects multiple organ systems and body compartments, including the central nervous system (CNS). Structural imaging studies of HIV patients' brains reveal

morphometric changes in the subcortical gray and white matter regions [77]. However, because of the relatively poor sensitivity of structural imaging to white-matter abnormalities in patients with mild HIV [78], the relationship between cognition and white-matter abnormalities in structural MRI has not been fully determined. These limitations can be overcome by DTI. Recent DTI studies have demonstrated white-matter abnormalities among patients with HIV even when fluid-attenuated inversion recovery (FLAIR) structural MRI scans failed to do so [79, 80]. Most recently, Ragin *et al.* [81] reported strong relationships between whole-brain fractional anisotropy and severity of dementia among a small cohort of HIV patients ($n = 6$).

In cases such as HIV infection, where the white-matter structural changes may be too subtle to detect with structural imaging, DTI can be used to quantify the changes.
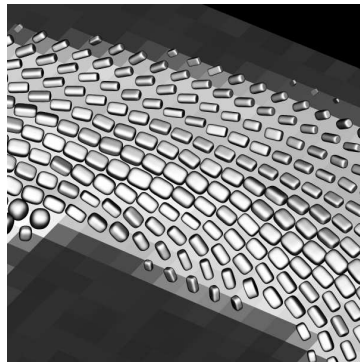


**Fig. 19.** Visualization of transmural twist of myofibers in canine myocardium, seen in a short axis slice. The edges of the superquadric glyphs help show the flat inclination at midwall and the differences among the eigenvalues at various locations.

### 4.4 Myocardial Structure

Diffusion tensor MRI can also be used to measure directionally constrained diffusion in tissues outside the nervous system. Understanding the complex muscular structure of the mammalian heart is another important application. The efficiency of the heart is due in part to its precise arrangement of myofibers (contractile muscle cells), especially the myocardium (the muscular wall) of the left ventricle, which is responsible for pumping blood to the rest of the body. The pattern of myofiber orientation in the myocardium is *helical*: between the epicardium and endocardium (outer and inner surface) there is roughly a 140-degree rotation of myofiber orientation, from $-70$ to $+70$ degrees. Computational simulations of heart dynamics require an accurate model of the myofibral orientation in order to model both the contractile mechanics of the myocardium and the pattern of electrical wave propagation within it [82]. The principal eigenvector as measured by DT-MRI has been

confirmed to align with the myofiber orientation [13, 14]. Recent work (see figure 19) has applied superquadric tensor glyphs to visualize the myofiber twisting and to inspect other anatomical features revealed by DT-MRI [83].

As is clear from the descriptions above, the applications of DTI are increasingly diverse. Associated with the breadth of application areas is a need for a wide variety of visualization techniques. Characterizing a tumor's effect on white matter integrity is based on fiber tracking, while the effect of neurodegenerative diseases may be quantified in terms of anisotropy metrics, and myocardial structure is described by a continuous rotation of the principal eigenvector.

## 5 Open Problems

Successfully applying DTI to new research areas and problem domains demands that visualization tools be flexible enough to support experimentation with the range of techniques so as to evaluate the appropriateness of each. This in turn requires that the modes of interaction efficiently support the exploration and parameter setting needed for creating visualizations, ideally in a manner friendly to application-area experts who may not be visualization experts.

In clinical practice, anisotropy indices, such as FA or trace (see section 3.1), are commonly used. Although, they show just a part of the information contained in the tensor, their visualization is similar to what radiologists are used to, and they are easy to understand and quantify. Other visualization techniques based on tractography or fiber tracking are popular probably due to the direct analogy between streamlines and fibers. However, the result of most of these techniques are very sensitive to input parameter values from the user (e.g., seed point). Important information can be missed if the user fails to give the right input when the underlying anatomy is not known. User independence is critical for statistical comparison and evaluation of diseases.

Some methods have tried to achieve more user independence by reconstructing linear structures in the whole volume. The main problems in this case are the computational cost and the huge amount of data to inspect. Therefore, the user should be able to navigate and explore the data interactively and in an intuitive way. For example, meaningful grouping or clustering of data can help navigation. Intuitive interaction for setting of parameters, such as transfer functions or thresholds (e.g., $c_l$ in fiber tracking to define areas with linear structure). Fiber tracking algorithms are prone to error, e.g., due to partial volume effect or numerical integration. Finding and visualizing uncertainty measures for the visualization algorithms could help to reduce the effect of this error.

Visualization techniques are commonly used as exploratory tools to identify measures for quantification. At the moment, measures for quantification only exist for anisotropy indices. Quantification is important to get clinical

acceptance. It is necessary to generate statistics and distinguish between diseased and normal, and to build models according to the different demographic and clinical variables that influence the results such as age and sex.

Validation is an important issue for DTI. There have been too few validation studies to be able to conclude that what is measured corresponds to the anatomy [1, 13]. At the moment and to our knowledge, there is no gold standard to validate the results of the techniques developed in this field.

An open problem of a different sort is the communication among different scientific fields. It is important for physicians and technicians to communicate in such a way that the necessary software and tools to advance in the clinical investigations for DTI are developed.

Finally, although not discussed in this chapter, a main research issue is the protocols for DTI data acquisition in order to improve quality and reduce scanning times. Furthermore, much research in image processing has been devoted to scalar but less to vector images, and little work has been done on image processing techniques for tensor data. Filters for noise removal, interpolation, feature extraction, etc. are of importance for the development of DTI (e.g., see the chapters on part E: Image Processing Methods for Tensor Fields). Second order diffusion tensor does not contain enough information to disambiguate areas where a voxel contains non-coherent linear structures. New representations for diffusion that show its more complex behavior are being researched. Visualization and image processing techniques would need to adapt to the complexity of this new data.

## 6 Summary and Conclusions

DTI allows the visualization of tissue microstructure (e.g., white matter or muscle) in vivo. Meaningful visualizations are crucial in analyzing and getting insight into multivariate data such as DTI. We have presented several visualization techniques developed in recent years. All visualization techniques have their advantages and disadvantages. Tensor glyphs are good for giving information at individual points, however, they typically do not relate tensor values well spatially. Fiber tracking methods relate values spatially by following major coherent fiber structures, but are prone to error due to, for example, partial volume effects, noise, and numerical integration inaccuracies. Fiber tracking methods usually reduce the dimensionality of the tensor from 6D to 3D, based in the assumption that linear structures are the most interesting to study. Other methods where the whole tensor is used to show the relationships between tensors suffer from cluttering. To acheive the goals of any given application, it is important to choose an appropiate visualization technique or combination of techniques. However, there are still limitations all techniques share, including the lack of robust parameter definition and a lack of ease-of-use for application-area experts who are not visualization experts.

We have presented some examples of the large variety of DTI applications. While much work has been devoted to white matter, DTI is also useful for studying muscle, including, in particular, the heart.

DTI is a relative young and exciting new field of research that brings together several disciplines. Research in each of these disciplines is crucial to achieve fruitful results in the application and use of DTI data. DTI visualization will clearly bring new insights in a number of research areas.

## Acknowledgments

## References

1. C. Pierpaoli, A.S. Barnett, S. Pajevic, A. Virta, and P.J. Basser. Validation of DT-MRI tractography in the descending motor pathways of human subjects. In *ISMRM, Conf. Proc.*, page 501, 2001.
2. D.S. Tuch, R.M. Weisskoff, J.W. Belliveau, and V.J. Wedeen. High angular resolution diffusion imaging of the human brain. In *ISMRM, Conf. Proc.*, page 321, 1999.
3. L.R. Frank. Anisotropy in high angular resolution diffusion-weighted MRI. *MR in Medicine*, 45(6):935–939, 2001.
4. A. Einstein. Über die von der molekularkinetischen Theorie der Wärme geforderte Bewegung von in ruhenden Flüssigkeiten suspendierten Teilchen. *Annalen der Physik*, 17:549–560, 1905.
5. E.M. Purcell, H.C. Torrey, and R.V. Pound. Resonance absorption by nuclear magnetic moments in a solid. *Physical Review*, 69:37–43, 1946.
6. F. Bloc. Nuclear induction. *Physical Review*, 70:460–474, 1946.
7. E.L. Hahn. Spin echoes. *Physical Review*, 80:580–594, 1950.
8. P.C. Lauterbur. Image formation by induced local interactions: examples employing nuclear magnetic resonance. *Nature*, 242:190–191, 1973.
9. G.J. Stanisz and R.M. Henkelman. Tissue compartments, exchange and diffusion. In *Workshop on Diffusion MRI: Biophysical Issues*, pages 34–37, 2002.
10. P.T. Callaghan. *Principles of Nuclear Magnetic Resonance Microscopy*. Oxford, 1993.
11. P.J. Basser, J. Mattiello, and D. LeBihan. Estimation of the effective self-diffusion tensor from the NMR spin echo. *MR Journal*, 103(3):247–54, 1994.

12. D. LeBihan. Molecular diffusion nuclear magnetic resonance imaging. *Magn. Reson. Quant.*, 17:1–30, 1991.
13. D.F. Scollan, A. Holmes, R. Winslow, and J. Forder. Histological validation of myocardial microstructure obtained from diffusion tensor magnetic resonance imaging. *Am J Physiol*, 275:2308–2318, 1998.
14. E.W. Hsu, A.L. Muzikant, S.A. Matulevicius, R.C. Penland, and C.S. Henriquez. Magnetic resonance myocardial fiber-orientation mapping with direct histological correlation. *Am J Physiol*, 274:1627–1634, 1998.
15. J.K. Jones. Determining and visualizing uncertainty in estimates of fiber orientation from diffusion tensor MRI. *MR in Medicine*, 49:7–12, 2003.
16. Y. Assaf, A. Mayk, and Y. Cohen. Displacement imaging of spinal cord using $q$-space diffusion-weighted MRI. *MR in Medicine*, 44:713–722, 2000.
17. D.S. Tuch, T.G. Reese, M.R. Wiegell, N. Makris, J.W. Belliveau, and V.J. Wedeen. High angular resolution diffusion imaging reveals intravoxel white matter fiber heterogeneity. *MR in Medicine*, 48(4):577–582, 2002.
18. L.R. Frank. Characterization of anisotropy in high angular resolution diffusion-weighted MRI. *MR in Medicine*, 47:1083–1099, 2002.
19. C. Pierpaoli and P.J. Basser. Toward a quantitative assessment of diffusion anisotropy. *MR in Medicine*, 36(6):893–906, 1996.
20. P.J. Basser and C. Pierpaoli. Microstructural features measured using diffusion tensor imaging. *MR Journal*, pages 209–219, 1996.
21. C.F. Westin, S. Peled, H. Gubjartsson, R. Kikinis, and F.A. Jolesz. Geometrical diffusion measures for MRI from tensor basis analysis. In *ISMRM, Conf. Proc.*, page 1742, April 1997.
22. P. van Gelderen, M.H. de Vleeschouwer, D. Despres, J. Pekar, P.C. van Zijl, and C.T. Moonen. Water diffusion and acute stroke. *MR in Medicine*, 31:154–63, 1994.
23. P. Douek, R. Turner, J. Pekar, N. Patronas, and D. LeBihan. MR color mapping of myelin fiber orientation. *J. Comput. Assist. Tomogr*, 15:923–929, 1991.
24. G. Kindlmann, D. Weinstein, and D.A. Hart. Strategies for direct volume rendering of diffusion tensor fields. *IEEE Trans. on Visualization and Computer Graphics*, 6(2):124–138, 2000.
25. R.A. Drebin, L. Carpenter, and P. Hanrahan. Volume rendering. *Computer Graphics, SIGGRAPH Proc.*, 22(4):65–74, 1988.
26. M. Levoy. Display of surfaces from volume data. *IEEE Computer Graphics & Applications*, 8(5):29–37, 1988.
27. W.E. Lorensen and H.E. Cline. Marching cubes: a high resolution 3D surface reconstruction algorithm. *Computer Graphics, SIGGRAPH Proc.*, 21(4):163–169, 1987.
28. A. Wenger, D. Keefe, S. Zhang, and D.H. Laidlaw. Interactive volume rendering of thin thread structures within multivalued scientific datasets. *IEEE Trans. on Visualization and Computer Graphics*, 2004. In press.
29. B. Cabral, N. Cam, and J. Foran. Accelerated volume rendering and tomographic reconstruction using texture mapping hardware. In *Symposium on Volume Visualization, Conf. Proc.*, pages 91–98, 1994.
30. J. Kniss, G. Kindlmann, and C. Hansen. Interactive volume rendering using multi-dimensional transfer functions and direct manipulation widgets. In *IEEE Visualization, Conf. Proc.*, pages 255–262, October 2001.
31. R. Fernando, editor. *GPU Gems: Programming Techniques, Tips, and Tricks for Real-Time Graphics*. Addison-Wesley, 2004.

32. D.H. Laidlaw, E.T. Ahrens, D. Kremers, M.J. Avalos, C. Readhead, and R.E. Jacobs. Visualizing diffusion tensor images of the mouse spinal cord. In *IEEE Visualization, Conf. Proc.*, pages 127–134, October 1998.

33. G. Kindlmann. Superquadric tensor glyphs. In *Proceedings IEEE TVCG/EG Symposium on Visualization 2004*, pages 147–154, May 2004.

34. F. Post, B. Vrolijk, H. Hauser, R.S. Laramee, and H. Doleisch. Feature extraction and visualization of flow fields. In *State-of-the-Art EG, Conf. Proc.*, pages 69–100, 2002.

35. J.J. van Wijk. Image based flow visualization. *Computer Graphics, SIGGRAPH Proc.*, 21(3):745–754, 2002.

36. S. Mori and P.C.M. van Zijl. Fiber tracking: principles and strategies – a technical review. *NMR in Biomedicine*, 15(7-8):468–480, 2002.

37. P.J. Basser, S. Pajevic, C. Pierpaoli, J. Duda, and A. Aldroubi. In vivo fiber tractography using DT-MRI data. *MR in Medicine*, 44:625–632, 2000.

38. A. Vilanova, G. Berenschot, and C. van Pul. DTI visualization with streamsurfaces and evenly-spaced volume seeding. In *VisSym '04 Joint EG – IEEE TCVG Symposium on Visualization, Conf. Proc.*, pages 173–182, 2004.

39. T. Delmarcelle and L Hesselink. Visualizing second order-tensor fields with hyperstreamlines. *IEEE Computer Graphics & Applications*, 13(4):25–33, 1993.

40. S. Zhang, C. Demiralp, and D.H. Laidlaw. Visualizing diffusion tensor MR images using streamtubes and streamsurfaces. *IEEE Trans. on Visualization and Computer Graphics*, 9(4):454–462, 2003.

41. D. Weinstein, G. Kindlmann, and E.C. Lundberg. Tensorlines: advection-diffusion based propagation through diffusion tensor fields. In *IEEE Visualization, Conf. Proc.*, pages 249–253, 1999.

42. L. Zhukov and A.H. Barr. Oriented tensor reconstruction: tracing neural pathways from diffusion tensor MRI. In *IEEE Visualization, Conf. Proc.*, pages 387–394, 2002.

43. B. Jobard and W. Lefer. Creating evenly-spaced streamlines of arbitrary density. In *Visualization in Scientific Computing. Proc. of the EG Workshop*, pages 43–56. Springer Verlag, 1997.

44. Z. Ding, J.C. Gore, and A.A. Anderson. Classification and quantification of neuronal fiber pathways using diffusion tensor MRI. *MR in Medicine*, 49(4):716–721, 2003.

45. A. Brun, H-J. Park, H. Knutsson, and C.-F. Westin. Coloring of DT-MRI fiber traces using Laplacian eigenmaps. In *EUROCAST, Conf. Proc.*, volume 2809 of *LNCS*, February 2003.

46. S. Zhang and D.H. Laidlaw. Hierarchical clustering of streamtubes. Technical Report CS-02-18, Brown University Computer Science Dep., August 2002.

47. I. Corouge, G. Gerig, and S. Gouttard. Towards a shape model of white matter fiber bundles using diffusion tensor MRI. In *IEEE International Symposium on Biomedical Imaging, Conf. Proc.*, pages 344–347, 2004.

48. G.J.M. Parker, C.A. Wheeker-Kingshott, and G.J. Barker. Distributed anatomical connectivity derived from diffusion tensor imaging. *IPMI, LNCS*, 2082:106–120, 2001.

49. A. Brun, M. Björnemo, R. Kikinis, and C.-F. Westin. White matter tractography using sequential importance sampling. In *ISMRM, Conf. Proc.*, May 2002.

50. P.G. Batchelor, D.L.G. Hill, F. Calamante, and D. Atkinson. Study of connectivity in the brain using the full diffusion tensor from MRI. In *IPMI, Conf. Proc.*, pages 121–133, 2001.

51. L. O'Donnell, S. Haker, and C.F. Westing. New approaches to estimation of white matter connectivity in diffusion tensor MRI: elliptic PDE's and geodesics in tensor-warped space. In *MICCAI, Conf. Proc.*, pages 459–466, 2002.

52. X. Zheng and A. Pang. Volume deformation for tensor visualization. In *IEEE Visualization, Conf. Proc.*, pages 379–386, 2002.

53. A. Sigfridsson, T. Ebbers, E. Heiberg, and L. Wigström. Tensor field visualisation using adaptive filtering of noise fields combined with glyph rendering. In *IEEE Visualization, Conf. Proc.*, pages 371–378, 2002.

54. X. Zheng and A. Pang. Hyperlic. In *IEEE Visualization, Conf. Proc.*, pages 249–256, 2003.

55. L. Hesselink, Y. Levy, and Y. Lavin. The topology of symmetric, second-order 3D tensor fields:. *IEEE Trans. on Visualization and Computer Graphics*, 3(1):1–11, 1997.

56. D. Akers, A. Sherbondy, R. Mackenzie, R. Dougherty, and B. Wandell. Exploration of the brain's white matter pathways with dynamic queries. In *IEEE Visualization, Conf. Proc.*, October 2004.

57. Ç. Demiralp, D.H. Laidlaw, C. Jackson, D. Keefe, and S. Zhang. Subjective usefulness of CAVE and fishtank VR display systems for a scientific visualization application. In *IEEE Visualization Poster Compendium*, 2003.

58. S. Zhang, Ç. Demiralp, D. Keefe, M. DaSilva, B.D. Greenberg, P.J. Basser, C. Pierpaoli, E.A. Chiocca, T.S. Deisboeck, and D.H. Laidlaw. An immersive virtual environment for DT-MRI volume visualization applications: a case study. In *IEEE Visualization, Conf. Proc.*, pages 437–440, October 2001.

59. R. Westerhausen, C. Walter, F. Kreuder, R.A. Wittling, E. Schweiger, and W. Wittling. The influence of handedness and gender on the microstructure of the human corpus callosum: a diffusion-tensor magnetic resonance imaging study. *Neuroscience Letters*, 351:99–102, 2003.

60. A. Pfefferbaum, E.V. Sullivan, M. Hedehus, K.O. Lim, E. Adalsteinsson, and M. Moseley. Age-related decline in brain white matter anisotropy measured with spatially corrected echo-planar diffusion tensor imaging. *MR in Medicine*, 44(2):259–268, 2000.

61. M. O'Sullivan, D.K. Jones, P.E. Summers, R.G. Morris, S.C.R. Williams, and H.S. Markus. Evidence for cortical disconnection as a mechanism of age-related cognitive decline. *Neurology*, 57:632–638, 2001.

62. M. Catani, D.K. Jones, R. Donato, and D.H. Ffytche. Occipito-temporal connections in the human brain. *Brain*, 126:2093–2107, 2003.

63. S. Wakana, H. Jiang, L.M. Nagae-Poetscher, P.C.M. van Zijl, and S. Mori. Fiber tract based atlas of human white matter anatomy. *Radiology*, 230:77–87, 2004.

64. D.-S. Kim, M. Kima, I. Ronena, E. Formisano, K.-H. Kima, K. Ugurbila, S. Moric, and R. Goebel. In vivo mapping of functional domains and axonal connectivity in cat visual cortex using magnetic resonance imaging. *MRI Journal*, 21(10):1131–1140, 2003.

65. J.J. Volpe. *Neurology of the Newborn*. W.B. Saunders Company, 1995.

66. K.O. Lim and J.A. Helpern. Neuropsychiatric applications of DTI – a review. *NMR in Biomedicine*, 15(7-8):587–593, 2002.

67. M.A. Horsfield and D.K. Jones. Applications of diffusion-weighted and diffusion tensor MRI to white matter diseases – a review. *NMR in Biomedicine*, 15(7-8):570–577, 2002.

68. M. Kubicki, C.-F. Westin, S.E. Maier, H. Mamata, M. Frumin, H. Ersner-Hershfield, R. Kikinis, F.A. Jolesz, R. McCarley, and M.E. Shenton. Diffusion tensor imaging and its application to neuropsychiatric disorders. *Harvard Rev. of Psychiatry*, 10:234–336, 2002.

69. P.C. Sundgren, Q. Dong, D. Gomez-Hassan, S.K. Mukherji, P. Maly, and R. Welsh. Diffusion tensor imaging of the brain: review of clinical applications. *Neuroradiology*, 46(5):339–350, 2004.

70. N.I. Bohnen, K. Radharkrishnan, B.P. O'Neil, and L.T. Kurland. *Descriptive and Analytic Epidemiology of Brain Tumours. Cancer of the Nervous System.* Blackwell Publishing, 2001.

71. U.C. Wieshmann, M.R. Symms, G.J. Parker, C.A. Clark, L. Lemieux, G.J. Barker, and S.D. Shorvon. Diffusion tensor imaging demonstrates deviation of fibres in normal appearing white matter adjacent to a brain tumour. *J. Neurol. Neurosurg. Psychiatry*, 68(4):501–3, 2000.

72. S. Mori, K. Frederiksen, P.C. van Zijl, B. Stieltjes, M.A. Kraut, M. Solaiyappa, and M.G. Pomper. Brain white matter anatomy of tumor patients evaluated with diffusion tensor imaging. *Ann. Neurol.*, 51(3):337–8, 2002.

73. C. Gossl, L. Fahrmeir, B. Putz, L.M. Auer, and D.P. Auer. Fiber tracking from DTI using linear state space models: detectability of the pyramidal tract. *Neuroimage*, 16(2):378–88, 2002.

74. B.P. Witwer, R. Moftakhar, K.M. Hasan, P. Deshmukh, V. Haughton, A. Field, K. Arfanakis, J. Noyes, C.H. Moritz, M.E. Meyerand, H.A. Rowley, A.L. Alexander, and B. Badie. Diffusion-tensor imaging of white matter tracts in patients with cerebral neoplasm. *J. Neurosurg.*, 97(3):568–75, 2002.

75. S. Zhang, M.E. Bastin, D.H. Laidlaw, S. Sinha, P.A. Armitage, and T.S. Deisboeck. Visualization and analysis of white matter structural asymmetry in diffusion tensor MR imaging data. *MR in Medicine*, 51(1):140–147, 2004.

76. D.J. Werring, C.A. Clark, G.J. Barker, A.J. Thompson, and D.H. Miller. Diffusion tensor imaging of lesions and normal-appearing white matter in multiple sclerosis. *Neurology*, 52:1626–1632, 1999.

77. R.H. Paul, R. Cohen, and R. Stern. Neurocognitive manifestations of HIV. *CNS Spectrums*, 7(12):860–866, 2003.

78. R.H. Paul, R. Cohen, B. Navia, and K. Tashima. Relationships between cognition and structural neuroimaging findings in adults with human immunodeficiency virus type-1. *Neurosci. Biobehav. Rev.*, 26(3):353–9, 2002.

79. N. Pomara, D.T. Crandall, S.J. Choi, G. Johnson, and K.O. Lim. White matter abnormalities in HIV-1 infection: a diffusion tensor imaging study. *Psychiatry Res.*, 106(1):15–24, 2001.

80. C.G. Filippi, A.M. Ulug, E. Ryan, S.J. Ferrando, and W. van Gorp. Diffusion tensor imaging of patients with HIV and normal-appearing white matter on MR images of the brain. *American Journal of Neuroradiology*, 22:277–283, 2001.

81. A. B. Ragin, P. Storey, B. A. Cohen, L. G. Epstein, and R. R. Edelman. Whole brain diffusion tensor imaging in HIV-associated cognitive impairment. *American Journal of Neuroradiology*, 25(2):195–200, 2004.

82. F.B. Sachse. *Computational Cardiology: Modeling of Anatomy, Electrophysiology, and Mechanics.* LNCS Vol. 2966. Springer Verlag, 2004.

83. D.B. Ennis, G. Kindlmann, P.A. Helm, I. Rodriguez, H. Wen, and E.R. McVeigh. Visualization of high-resolution myocardial strain and diffusion tensors using superquadric glyphs. In *ISMRM, Conf. Proc.*, May 2004.
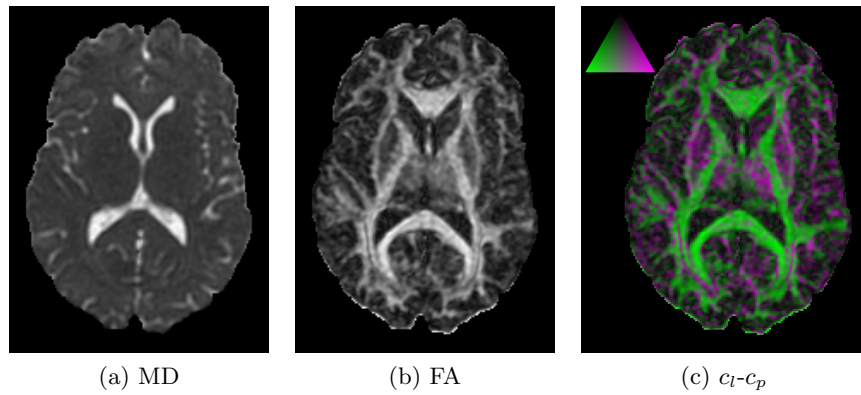
(a) MD                    (b) FA                    (c) $c_l$-$c_p$

**Fig. 4.** Different shape metrics applied to one slice of a brain DTI scan.



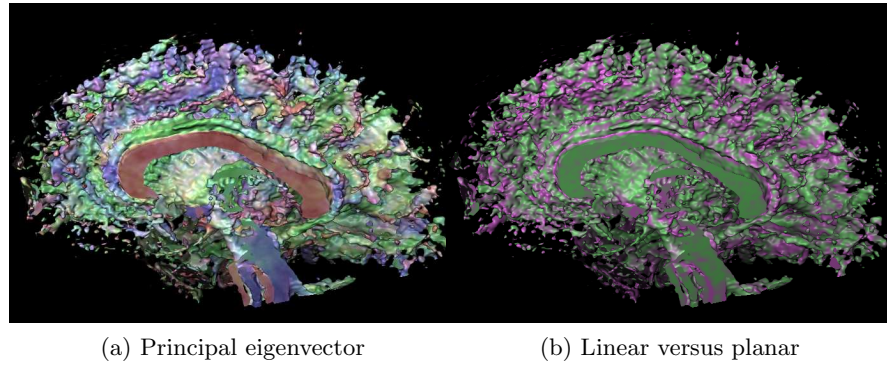(a) Principal eigenvector          (b) Linear versus planar

**Fig. 6.** Volume renderings of half a brain scan, (a) colored according to orientation of principal eigenvector; (b) the distribution of linear (green) and planar (magenta) anisotropy. Surface is defined by FA = 0.4.
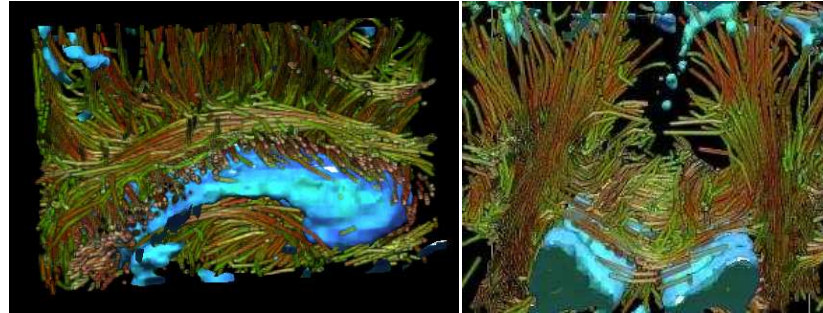
**Fig. 7.** Interactive volume renderings of a human brain data set. The volume renderings (top) show collections of threads consistent with major white-matter structures: IC=internal capsule, CR=corona radiata, CB=cingulum bundle, CC=corpus callosum diagrammed on the bottom. Components of the tensor-valued data control thread orientation, color, and density. Direct volume rendering simultaneously shows in blue the cerebral spinal fluid in the ventricles (labeled V) and some sulci for anatomical context.



(a)                                  (b)

**Fig. 8.** Brush strokes illustrate the orientation and magnitude of the diffusion: background color and texture-map show additional information



(a) Boxes              (b) Ellipsoids              (c) Superquadrics

**Fig. 9.** A portion of a brain DTI scan as visualized by three different glyph methods (overall glyph sizes have been normalized).

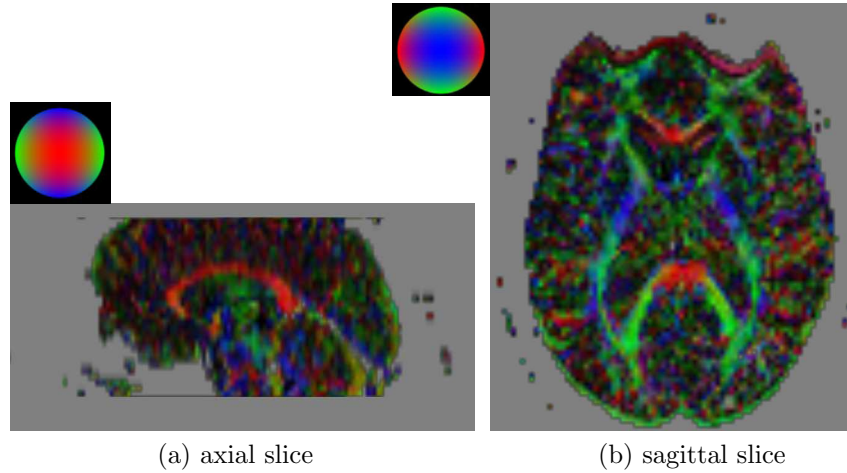(a) axial slice                         (b) sagittal slice
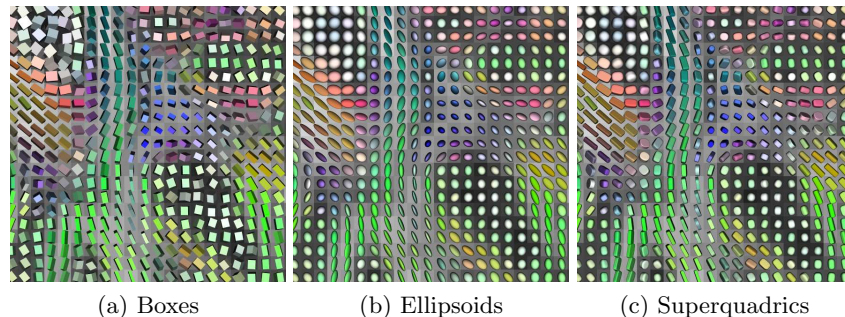
**Fig. 10.** Mapping of $\mathbf{e_1}$ to the RGB channel shown in 2D slices of a healthy volunteer brain.
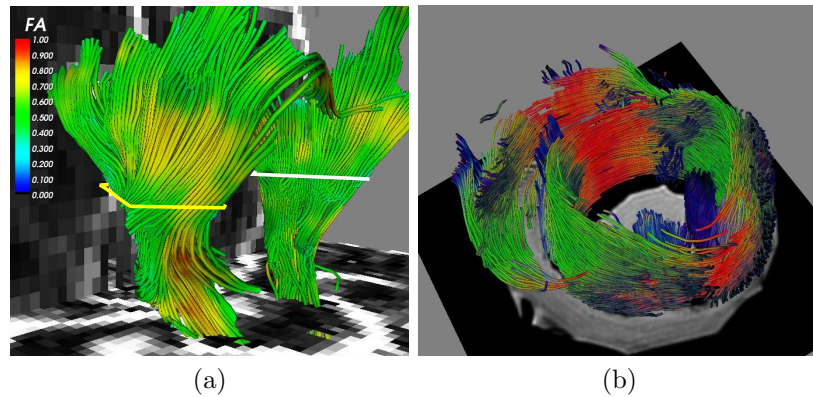


(a)                                     (b)

**Fig. 11.** (a) Streamline tracing using two ROIs to trace the corona radiata in a data set of a healthy volunteer brain. (b) Streamlines in a data set of a goat heart using the seeding technique of Vilanova *et al.* [38].
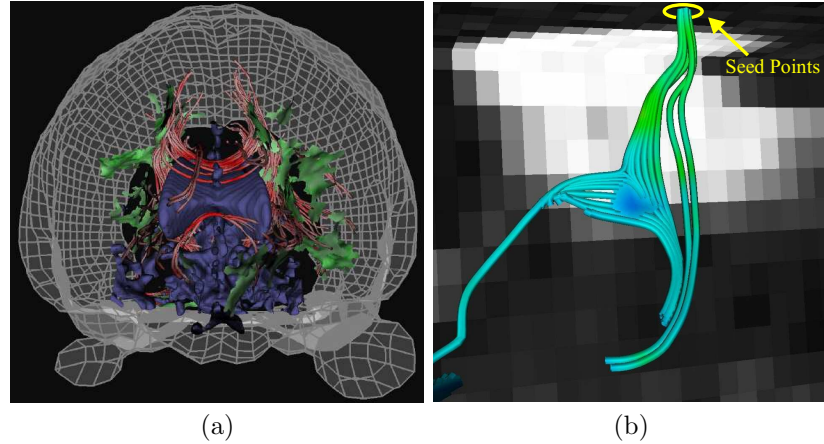
(a)                                        (b)

**Fig. 14.** Examples of streamsurfaces: (a) red streamlines (represented as cylinders) and green streamsurfaces generated using the method of Zhang *et al.* [40] show linear and planar anisotropy, respectively, together with anatomical landmarks for context; (b) Streamlines using seed points (yellow region) trace streamsurfaces and show the possible prolongation of the fiber bundle, generated using the algorithm of Vilanova *et al.* [38].
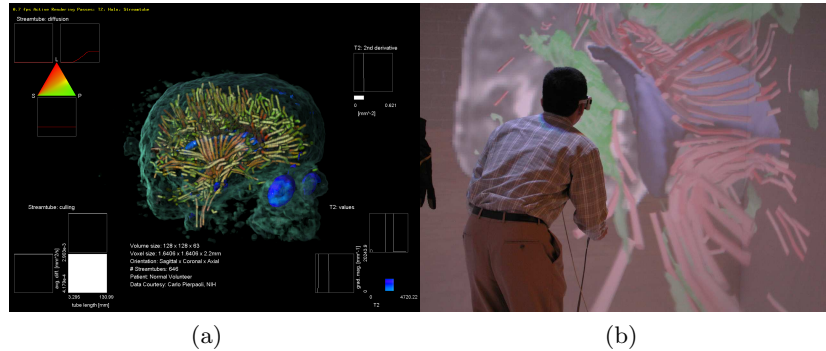


(a)                                        (b)

**Fig. 15.** (a) An interactive exploration tool for DTI volume rendering. Clockwise from upper left are a 2D barycentric widget, a 1D widget, a 2D Cartesian widget, and a 2D Cartesian culling widget. (b) A user explores a complex 3D model in a virtual reality CAVE.
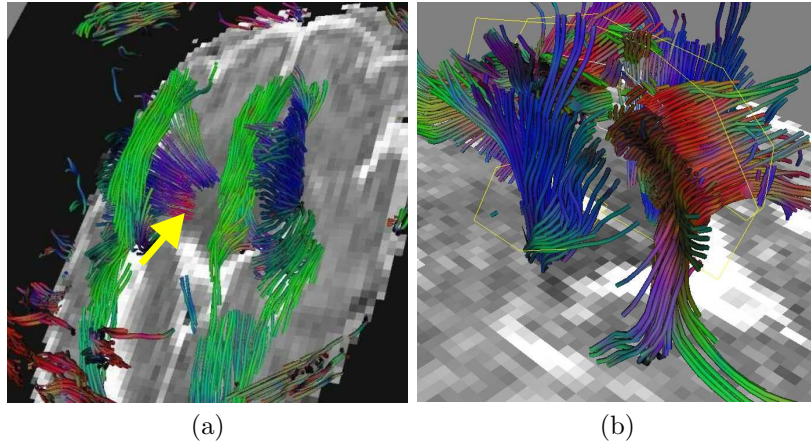
**Fig. 16.** Studies of white matter fibers in neonatal brains with different data sets. (a) Premature neonate lacking corpus callosum (see arrow), (b) full-term neonate where no fiber abnormalities were found. Corpus callosum and corona radiata are seen.
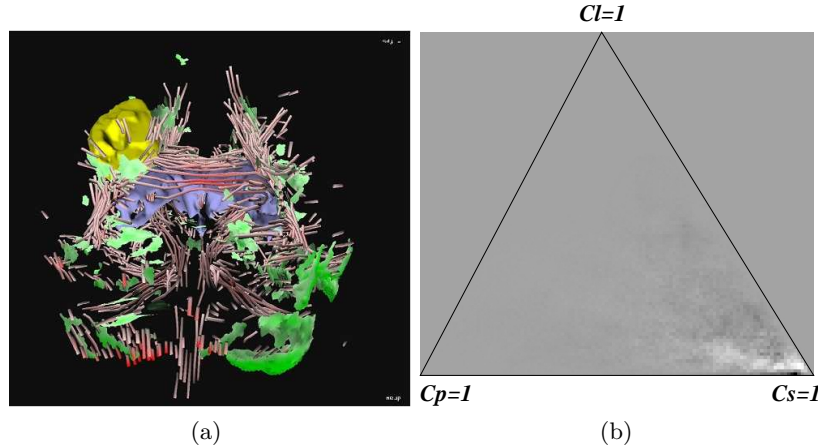


**Fig. 17.** Visual exploration and quantitative analysis of a cancerous brain. (a) A 3D visualization showing streamtubes and streamsurfaces as well as tumor and ventricles. (b) The difference histogram obtained by subtracting normalized barycentric histograms calculated from tumor-bearing and contralateral sections. Here zero maps to medium gray because the difference is signed. Note that the most striking difference occurs near the $c_s = 1$ vertex.
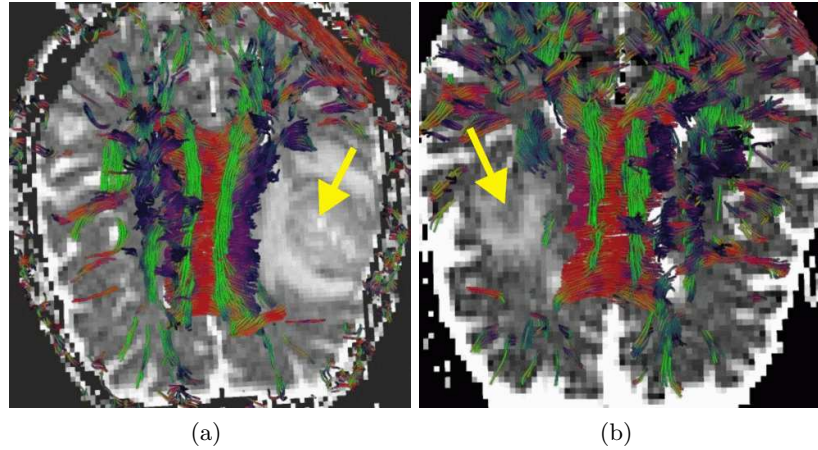
(a)                                (b)

**Fig. 18.** Two cases of adult tumor brain. (a) Fibers are pushed by the tumor. (b) No fibers are in the tumor area, indicating the destruction of neural structures there.
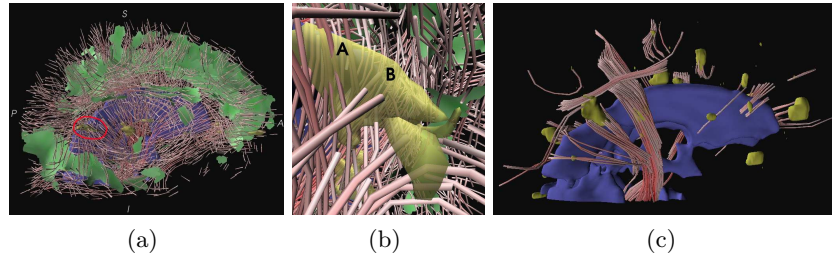


(a)                    (b)                    (c)

**Fig. 19.** Visualization of coregistered DTI and MS lesion models. (a) The whole brain with streamtubes, streamsurfaces, lesion masks and ventricles. (b) A closeup view of white matter fibers near the MS lesions. The streamtubes around the lesion area give some clues about white matter structural changes there. (c) The same brain and view as (a) but showing only streamtubes that contact the lesions, thus clarifying the white matter structures involved.